PERGAMON International Journal of Multiphase Flow 24 (1998) 1359–1382

International Journal of Multiphase Flow

Sediment flow in inclined vessels calculated using a multiphase particle-in-cell model for dense particle flows

D.M. Snider[a,*], P.J. O'Rourke[b], M.J. Andrews[c]

[a]*Flow Analysis, 6504 Avenida La Costa NE, Albuquerque, NM 87109, USA*
[b]*Theoretical Division, Los Alamos National Laboratory, Los Alamos, NM 87545, USA*
[c]*Mechanical Engineering Department, Texas A&M University, College Station, TX 77843, USA*

Received 22 September 1997; received in revised form 20 February 1998

Abstract

Sedimentation of particles in an inclined vessel is predicted using a two-dimensional, incompressible, multiphase particle-in-cell (MP-PIC) method. The numerical technique solves the governing equations of the fluid phase using a continuum model and those of the particle phase using a Lagrangian model. Mapping particle properties to an Eulerian grid and then mapping back computed stress tensors to particle positions allows a complete solution of sedimentation from a dilute mixture to close-pack. The solution scheme allows for distributions of types, sizes and density of particles, with no numerical diffusion from the Lagrangian particle calculations. The MP-PIC solution method captures the physics of inclined sedimentation which includes the clarified fluid layer under the upper wall, a dense mixture layer above the bottom wall, and instabilities which produce waves at the clarified fluid and suspension interface. Measured and calculated sedimentation rates are in good agreement.

Keywords: Two-phase flow; Eulerian; Lagrangian; Sedimentation

1. Introduction

The separation of particles from a fluid by means of gravity is an important step in many industrial processes as well as in the environment. Homogenous, batch sedimentation begins with a uniform distribution of suspended particles in a container. If left alone, the particles separate from the fluid into distinct regions of particles that depend on the particle densities and sizes as illustrated in Fig. 1 for a bimodal suspension. A suspension with a variety of

* Corresponding author.

0301-9322/98/$19.00
PII: S0301-9322(98)00030-5

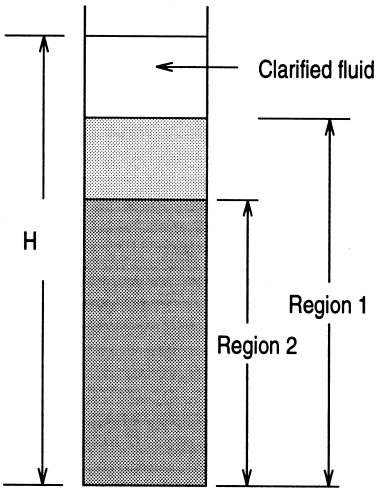

Fig. 1. Illustration of a vertical bimodal suspension.

particle sizes and densities will form multiple regions, where each region above the previous region contains one less species, where a species is a group of particles with near the same particle size and density. The top of the vessel will be clear fluid (providing particle densities are greater than the fluid density) and the bottom of the vessel will contain all species. In cases where there is a large variation between sizes and/or density of species, the regions are distinct and separated by strong concentration gradients. A monodisperse mixture containing one size and density particle forms a single region of suspended particles under a clear fluid. Davis and Acrivos (1985) and Al-Naafa' and Selim (1989) provide reviews of experiments and analysis of polydisperse suspensions. Richardson and Zaki (1954) gave an empirical equation for the settling velocity of a monodisperse mixture which compares well with data. The settling velocity is

$$U_s = U_o(1 - \theta_p)^{n-1} \tag{1}$$

where U_o is the terminal velocity, θ_p is the particle volume fraction and n is a constant about 5. Mirza and Richardson (1978) extended the empirical relation to polydisperse suspensions. Al-Naafa' and Selim (1989), using conservation of mass and empirical settling velocities, provided an analytical model that predicts well the settling of polydisperse suspensions. A calculation by Shih et al. (1987) for bimodal settling using a one-dimensional, multifluid, numerical solution compared well with experimental data, and Andrews and O'Rourke (1995) presented an accurate prediction of polydisperse settling of a suspension using a one-dimensional MP-PIC numerical method.

Boycott (1920) reported that by tilting the container, corpuscles separated from blood quicker than when the container was vertical. The settling in a tilted container is illustrated in Fig. 2. Position A in Fig. 2 is the distinct horizontal interface between the clear fluid and mixture (B). The initial height of the mixture is H, the transient height of the interface is h and the vessel width is b. A thin layer of upward flowing clear fluid forms (C) at the downward-facing surface, and concentrated particles flow down the upward-facing surface (D). Many

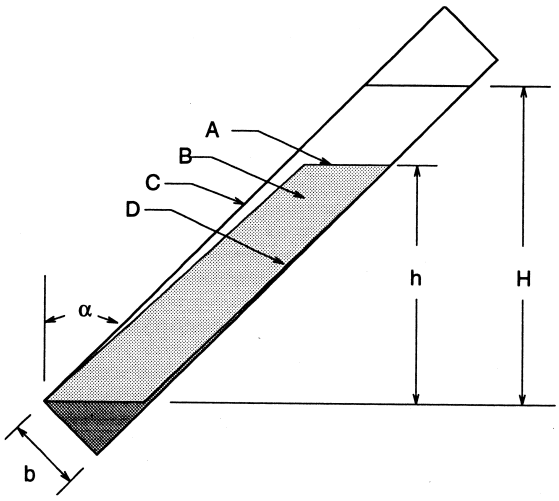

Fig. 2. Illustration of a tilted vessel suspension.

investigators have studied tilted container phenomena and have provided analytical models of the settling. Davis and Acrivos (1985) and Kapoor and Acrivos (1995) provide reviews of inclined sedimentation. Ponder (1925) and Nakumura and Kuroda (1937) postulated that for tilted containers the horizontal mixture interface and the interface under the downward facing surface fall at the same mixture velocity as for a vertical container. In the analytical model, the thin fluid film under the downward facing surface was added directly to the clear fluid above the top of the mixture. The settling rate is

$$\mathrm{d}h/\mathrm{d}t = -U_{\mathrm{o}}[1 + (h/b)\sin\alpha], \tag{2}$$

where α is the angle of inclination and U_{o} is the mixture interface velocity for a vertical vessel. Acrivos and Herbolzheimer (1979) showed that the simple settling model given by Ponder et al. was accurate for a monodisperse suspension, at low Reynolds number, with an initial uniform particle distribution, a large Grashoff number when compared with the Reynolds number, and a stable interface between clear fluid and suspension. Kinosita (1949) noted that particles in a tilted container did not settle through a quiescent fluid as in a vertical container, but that strong convective currents form a vortex in the suspended phase with particle velocities as high as 100 times the sedimentation velocities. The dynamic nature of inclined sedimentation is further shown by the observed instabilities at the interface between the clear fluid flowing up under the downward-facing surface and the particle mixture. The instabilities are seen as waves at the interface in photographs by Herbolzheimer (1983).

The analytical and semi-empirical predictive methods developed over the years compare well with data and have provided insight into the mixing process; yet these methods are only suitable for simple geometry and special conditions. To date, the authors do not know of any numerical calculation which captures the mixing behavior of inclined sedimentation. One major difficulty to obtain numerical solutions in polydisperse suspensions is the number of equations required to model each of the species. For a multi-fluid solution, each species (different size and density particle) requires a set of conservation equations. Numerical methods are required

to predict this common industrial and environment process for polydisperse mixtures in complex geometries over a wide range of conditions. In this paper, a unique numerical scheme which predicts the dynamic inclined sedimentation and the more static vertical sedimentation with practically an unlimited range in particle sizes and densities is presented. Results from the numerical calculations are compared with experimental data.

2. Solution method

Mathematical models of separated particulate multiphase flow have used either a continuum approach for all phases (Gidaspow, 1986; Batchelor, 1988) or a continuum for the fluid and a Lagrangian model for particle (Amsden et al., 1989). The continuum/continuum model readily allows modeling of particle-particle stresses in dense particle flows using spatial gradients of particle volume fractions (Batchelor, 1988; Gidaspow, 1994). However, modeling a distribution of types and sizes of particles complicates the continuum formulation because separate continuity and momentum equations must be solved for each size and type (Risk, 1993; Gidaspow, 1994). Using a continuum model for the fluid phase and a Lagrangian model for particle phase allows economical solution for flows with a wide range of particle types, sizes, shapes and velocities (O'Rourke, 1981; Gidaspow, 1994). However, the collision frequency is high for volume fractions above 5% and cannot be realistically resolved by current Lagrangian collision calculations (O'Rourke, 1981).

The MP-IPC method presented here provides a numerical scheme whereby the particle phase is treated as both a continuum and as discrete particles, gaining the best of both methods. Particle properties are mapped to and from an Eulerian grid. While on the grid, continuum derivatives that treat the particle phase as a fluid are evaluated and then mapped back to the individual particles. The result of this procedure is a computational technique for multiphase flow that can handle particle loadings ranging from dilute to dense with a distribution of particle materials and sizes.

The governing equations for the continuum and particles are given. The fluid phase is incompressible and inviscid, and fluid and particle phases are isothermal. The fluid or Eulerian variables are denoted by subscript f, and the particle or Lagrangian variables are denoted by subscript p.

3. Governing equations

3.1. The fluid phase

The continuity equation for the fluid with no interphase mass transfer is

$$\frac{\partial \theta_f}{\partial t} + \nabla \cdot (\theta_f \mathbf{u}_f) = 0, \tag{3}$$

where $\mathbf{u}_f$ is the fluid velocity and θ_f is the fluid volume fraction.

The momentum equation for the fluid is

$$\frac{\partial(\theta_f \mathbf{u}_f)}{\partial t} + \nabla \cdot (\theta_f \mathbf{u}_f \mathbf{u}_f) = -\frac{1}{\rho_f}\nabla p - \frac{1}{\rho_f}\mathbf{F} + \theta_f \boldsymbol{g}, \tag{4}$$

where ρ_f is fluid density, p is fluid pressure and $\boldsymbol{g}$ is the gravitational acceleration. $\mathbf{F}$ is the rate of momentum exchange per volume between the fluid and particles phases. The momentum equation neglects viscous molecular diffusion in the fluid but retains the viscous drag between particles and fluid through the interphase drag force, $\mathbf{F}$.

3.2. The particulate phase

The dynamics of the particle is described using the particle probability distribution function $\phi(\mathbf{x}, \mathbf{u}_p, \rho_p, V_p, t)$, where $\mathbf{x}$ is the particle position, $\mathbf{u}_p$ is the particle velocity, ρ_p is the particle density and V_p is the particle volume (Andrews and O'Rourke, 1996). For the present it is assumed that the mass of each particle is constant in time (no mass transfer between particles or to the fluid), but particles may have a range of sizes and densities. The probability function integrated over velocity and mass gives the probable number of particles per unit volume at $\mathbf{x}$ and t in the interval $(\mathbf{u}_p, \mathbf{u}_p + \mathrm{d}\mathbf{u}_p)$, $(\rho_p, \rho_p + \mathrm{d}\rho_p)$ and $(V_p, V_p + \mathrm{d}V_p)$. The particle volume fraction is defined from the particle distribution function as

$$\theta_p = \int\int\int \phi V_p \, \mathrm{d}V_p \, \mathrm{d}\rho_p \, \mathrm{d}\mathbf{u}_p. \tag{5}$$

The sum of volume fractions of fluid and particle phases must equal unity, $\theta_p + \theta_f = 1$.

The time evolution of ϕ is obtained by solving a Liouville equation for the particle distribution function (Williams, 1985)

$$\frac{\partial \phi}{\partial t} + \nabla \cdot (\phi \mathbf{u}_p) + \nabla_{\mathbf{u}_p} \cdot (\phi \mathbf{A}) = 0, \tag{6}$$

where the particle acceleration, $\mathbf{A} = \mathrm{d}\mathbf{u}_p/\mathrm{d}t$, is given by

$$\mathbf{A} = D_p(\mathbf{u}_f - \mathbf{u}_p) - \frac{1}{\rho_p}\nabla p + \mathbf{g} - \frac{1}{\theta_p \rho_p}\nabla \tau. \tag{7}$$

The terms in (7) represent acceleration due to aerodynamic drag, pressure gradient, gravity and gradients in the interparticle stress, τ.

The drag model is a modified Stoke's equation with a hindrance term to account for velocity and concentration of particles. The drag coefficient is

$$D_p = C_d \frac{3}{8}\frac{\rho_f}{\rho_p}\frac{|\,\mathbf{u}_f - \mathbf{u}_p\,|}{r}, \text{ where } C_d = \frac{24}{Re}\left(\theta_f^{-2.65} + \frac{1}{6}Re^{2/3}\theta_f^{-1.78}\right). \tag{8}$$

The Reynolds number is defined as $Re = 2\rho_f|\mathbf{u}_f - \mathbf{u}_p|r/\mu_f$, where μ_f is the fluid viscosity and the particle radius is $r = (3\,V_p/4\pi)^{1/3}$. Small particles have a higher interphase drag than larger

particles, and the interphase drag term is the mechanism which separates a polydisperse suspension of different size particles into layers.

Collisions between particles are modeled by an isotropic interparticle stress where the off diagonal elements of the stress tensor are neglected. The particle stress is from Harris and Crighton (1994)

$$\tau = \frac{P_s \theta_p^{\beta}}{\theta_{cp} - \theta_p}, \tag{9}$$

where the constant P_s has units of pressure, and θ_{cp} is the particle volume fraction at close packing. The particle stress equation depends only on the concentration of particles and neglects the size and velocity of particles. A more detailed model of the full stress tensor is relegated to future work. Auzeris et al. (1988) recommend $2 \leqslant \beta \leqslant 5$, and $\beta = 3$ was used for the inclined sedimentation calculations in this study.

The interphase momentum transfer function per volume is obtained from

$$\mathbf{F} = \int\int\int \phi V_p \rho_p \left[D_p(\mathbf{u}_f - \mathbf{u}_p) - \frac{1}{\rho_p} \nabla p \right] \mathrm{d}V_p \, \mathrm{d}\rho_p \, \mathrm{d}\mathbf{u}_p. \tag{10}$$

4. Interpolation functions

Particle properties are mapped to and from the Eulerian grid using a bilinear interpolation function as part of the numerical solution. Because a staggered grid is employed, scalar properties, defined at cell centers, are mapped with one set of interpolation functions, and face center velocities are mapped with another set. The bilinear interpolation function is formed from the product of linear interpolation functions in the x and y directions, $S_{i,j} = S_{x_i} S_{y_j}$.

The S_{x_i} and S_{y_i} symmetric, saw-tooth functions are unity at a node and linearly decrease to zero at their neighbor nodes. The bilinear interpolation function, $S_{i,j}$, which is dependent on both x and y–coordinates, is unity at the cell center (i,j) and decreases to zero at the surrounding eight nodes. For a Cartesian grid, four grid nodes are used to interpolate a grid property to a particle in two dimensions. Fig. 3 shows nodes used to interpolate the scalar property to a particle position. The sum of the interpolation functions is unity, $\Sigma_{\zeta=1}^{4} S(\mathbf{x}_p)\zeta = 1$, where ζ is the index on the four Eulerian nodes bounding the particle [(i,j), $(i+1, j)$, $(i+1, j+1)$, and $(i,j+1)$].

The particle volume fraction, θ_p, on the Eulerian grid is calculated by

$$\theta_{p_{i,j}} = \frac{1}{V_{i,j}} \sum_{p} N_p V_p S(\mathbf{x}_p)_{i,j}, \tag{11}$$

where N_p is the number of particles in a parcel. The Eulerian cell volume is $V_{i,j}$.

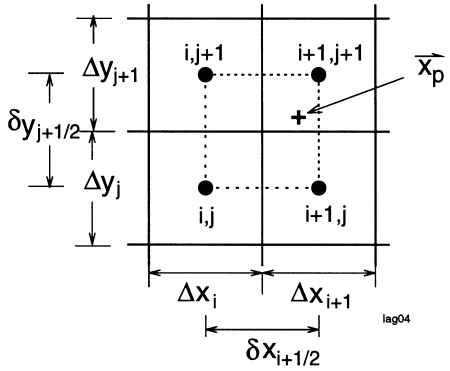

Fig. 3. Interpolation from Eulerian grid to a particle position.

5. Numerical method

The governing equations for fluid and particles are solved on the computer. A computational particle method is used to solve for the particle distribution rather than direct solution of the Liouville equation. Particle properties are mapped to and from the grid using the bilinear interpolation functions. The incompressible, two-dimensional continuum equations are solved using a finite volume method. The numerical method implicitly couples phases through the interphase momentum transfer.

The numerical scheme uses an implicit calculation to overcome signal-wave limits on the computational time step. If the solution scheme was explicit, the numerical time step would be limited by the Courant–Friedrichs–Lewy condition and especially by stress waves from the interparticle stress (Gidaspow, 1986). In two dimensions, the implicit solution gives four sets of equations containing two velocities, pressure and particle volume fraction. A set of equations is solved for one variable while holding the other variables fixed. Coupling between implicit variables is introduced by iterative solution of the sets of equations. As will be discussed later, the particle volume fraction needs to be solved in continuum form while iterating in the implicit loop.

5.1. Particle equations

Particles are grouped into computational parcels each containing N_p particles with identical density, ρ_p, volume, V_p, and velocity, $\mathbf{u}_p$, located at position, $\mathbf{x}_p$. The Liouville Eq. (6) is the mathematical expression of conservation of particle numbers in volumes moving along dynamic trajectories in particle phase space. Thus the number of particles N_p associated with a parcel is constant in time. By assumption, there is no mass exchange between particles, and a particle's mass, m_p, is constant. The particle velocity equation is from integration of Eq. (7) which is implicitly approximated by

$$\mathbf{u}_p^{n+1} = \frac{\mathbf{u}_p^n + \Delta t\left[D_p\mathbf{u}_{f,p}^{n+1} - \frac{1}{\rho_p}\nabla p_p^{n+1} - \frac{1}{\rho_p\theta_p}\nabla\tau_p^{n+1} + \boldsymbol{g}\right]}{1 + \Delta t D_p}, \tag{12}$$

where $\mathbf{u}_{\mathrm{f,p}}^{n+1}$ is the interpolated implicit fluid velocity at the particle location, $\nabla p_{\mathrm{p}}^{n+1}$ is the interpolated implicit pressure gradient at the particle location, $\nabla \tau_{\mathrm{p}}^{n+1}$ is the interpolated implicit particle stress gradient at the particle location, $\boldsymbol{g}$ is gravity, and D_{p} is the drag coefficient. Particle positions are calculated from

$$\mathbf{x}_{\mathrm{p}}^{n+1} = \mathbf{x}_{\mathrm{p}}^{n} + \Delta t \mathbf{u}_{\mathrm{p}}^{n+1}. \tag{13}$$

5.2. Fluid equations

The numerical scheme uses a finite volume method with staggered scalar and momentum nodes. The two-dimensional finite volume approximation uses a rectangular or cylindrical grid where scalar variables, pressure and volume fraction, are defined at cell centers and velocities are defined at volume surfaces staggered between cell centers. The time derivative is approximated by a backward difference, convective terms are approximated by upwind differencing and gradients are approximated by a backward difference. The algebraic form of the fluid equations has been given by Anderson et al. (1984), Patankar (1980) and others and is not repeated here.

The particle phase is implicitly coupled to the fluid phase through the interphase drag force. The interphase momentum transfer from particles to fluid is

$$\mathbf{F}_{i+1/2,j}^{n+1} = \frac{1}{V_{i+1/2,j}} \sum_{p} S_{i+1/2,j} \left[D_{\mathrm{p}} (\mathbf{u}_{\mathrm{f,p}}^{n+1} - \mathbf{u}_{\mathrm{p}}^{n}) - \frac{1}{\rho_{\mathrm{p}}} \nabla p_{\mathrm{p}}^{n+1} \right] N_{\mathrm{p}} m_{\mathrm{p}}, \tag{14}$$

where m_{p} is the mass of a particle. The fluid velocity, $\mathbf{u}_{\mathrm{f,p}}^{n+1}$, at a particle position is an interpolated quantity involving neighboring grid velocities. Similarly, the interpolated pressure gradient $\nabla p_{\mathrm{p}}^{n+1}$ and particle stress gradient $\nabla \tau_{\mathrm{p}}^{n+1}$ introduce neighbor quantities. Eq. (14) involves an interpolation to a particle position and then a mapping back to the Eulerian grid. The interpolation to the grid can be obtained by multiplying the two interpolation functions by the variable. Alternatively, it can be noted that the drag term mapped to the grid can be written as

$$\sum_{p} S_{i+1/2,j} \left[D_{\mathrm{p}} (\mathbf{u}_{\mathrm{f,p}}^{n+1} - \mathbf{u}_{\mathrm{p}}^{n}) \right] N_{\mathrm{p}} m_{\mathrm{p}} = \sum_{p} S_{i+1/2,j} \left[D_{\mathrm{p}} \sum_{\zeta=1}^{4} S\zeta (\mathbf{u}_{\mathrm{f}\zeta}^{n+1} - \mathbf{u}_{\mathrm{p}}^{n}) \right] N_{\mathrm{p}} m_{\mathrm{p}}, \tag{15}$$

where summation of ζ is over the four staggered grid nodes supporting interpolation in two dimensions. The quantity in brackets in (15) is the aerodynamic drag applied to a particle. From conservation of momentum, the net momentum transfer between particle and fluid is zero. It can be reasoned that the momentum from a node to a parcel (for example the $[D_{\mathrm{p}} S_{i,j} (\mathbf{u}_{\mathrm{f}_{i,j}}^{n+1} - \mathbf{u}_{\mathrm{p}}^{n}) N_{\mathrm{p}} m_{\mathrm{p}}]$ is the momentum transfer from node (i, j) to particle p) must be the same as the momentum transfer from a particle to the node. Therefore, for the x-momentum, the product of interpolation functions is defined as

$$S_{i+1/2,j} S_{k+1/2,j} = \begin{matrix} 0 & \text{if } i \neq k \\ S_i + 1/2, j & \text{if } i = k \end{matrix}. \tag{16}$$

Both the multiplication of the two bilinear interpolation functions given in Eq. (15) and the mapping given by Eq. (16) conserve momentum. The interpolation from particle to grid given by Eq. (16) has the advantage that it is less diffusive, reduces the number of neighbor velocities in an equation, and increases diagonal dominance of the equation sets. The product of interpolation functions given by (16) is used in this study.

The interphase momentum, **F**, given by Eq. (14) is substituted into the numerical form of fluid momentum Eq. (4) and summed over all particles. The resulting velocity equation, using the interpolation product definition (16), is

$$\begin{aligned}&\frac{V_\zeta \rho_\mathrm{f}(\theta_\mathrm{f}\mathbf{u}_\mathrm{f})_\zeta^{n+1}}{\Delta t}+(\mathbf{u}_\mathrm{f})_\zeta^{n+1}\sum_p m_\mathrm{p}N_\mathrm{p}S_\zeta(\mathbf{x}_\mathrm{p})D_\mathrm{p}\\&=\frac{V_\zeta \rho_\mathrm{f}(\theta_\mathrm{f}\mathbf{u}_\mathrm{f})_\zeta^{n}}{\Delta t}-\mathrm{conv}_\zeta^{n+1}-V_\zeta\nabla p_\zeta^{n+1}+V_\zeta\rho_\mathrm{f}\theta_\mathrm{f}^n\zeta\boldsymbol{g}\\&\qquad+\sum_p\frac{m_\mathrm{p}N_\mathrm{p}S_\zeta(\mathbf{x}_\mathrm{p})}{\rho_\mathrm{p}}\nabla p_\zeta^{n+1}+\sum_p m_\mathrm{p}N_\mathrm{p}S_\zeta(\mathbf{x}_\mathrm{p})D_\mathrm{p}\mathbf{u}_\mathrm{p}^u.\end{aligned}\tag{17}$$

The abbreviated subscript, ζ, corresponds to a face center, and conv is the convective term. The u-velocity in terms of coefficients on neighbor velocities and on pressure is

$$u_{i+1/2,j}^{n+1}=\sum_{k=1}^{9}e_{i+1/2,j}^k p_k^{n+1}+\sum_{k=1}^{5}f_{i+1/2,j}^k u_k^{n+1}+C_{u_{i+1/2,j}},\tag{18}$$

where e and f are coefficients formed from old time values, and C_u is a constant. The summation index k, implies the neighbor nodes. A 6 point stencil arises for the velocity and a 9 point stencil arises for the pressure.

6. Computation of particle volume fraction on the Eulerian grid

It is not prudent to update the volume fraction within an iteration loop where particles are continuously summed as given by (11). Andrews and O'Rourke (1996) and Snider et al. (1997) presented a method of approximating the new-time volume fraction on the Eulerian grid using explicit coefficients. In the method, a time step begins by estimating new particle positions using the old particle velocities:

$$\tilde{\mathbf{x}}_\mathrm{p}=\mathbf{x}_\mathrm{p}^n+\mathbf{u}_\mathrm{p}^n\Delta t.\tag{19}$$

$$\tilde{\theta}_{\mathrm{p}_{i,j}}=\frac{1}{V_{i,j}}\sum_p\frac{m_\mathrm{p}N_\mathrm{p}}{\rho_\mathrm{p}}S_{i,j}(\tilde{\mathbf{x}}_\mathrm{p}).\tag{20}$$

The volume fraction at the end of the time step is estimated using a Taylor series expansion of (19) about the intermediate particle position $\tilde{\mathbf{x}}_\mathrm{p}$ and retaining linear terms:

$$\theta_{\mathrm{p}_{i,j}}^{n+1} \approx \tilde{\theta}_{\mathrm{p}_{i,j}} + \frac{1}{V_{ij}} \sum_{p} \frac{m_{\mathrm{p}} N_{\mathrm{p}}}{\rho_{\mathrm{p}}} \nabla S_{i,j}(\tilde{\mathbf{x}}_{\mathrm{p}}) \cdot (\mathbf{x}_{\mathrm{p}}^{n+1} - \tilde{\mathbf{x}}_{\mathrm{p}}). \tag{21}$$

Substituting $\mathbf{x}_{\mathrm{p}}^{n+1}$ from (13), $\tilde{\mathbf{x}}_{\mathrm{p}}$ from (19), and $\mathbf{u}_{\mathrm{p}}^{n+1}$ from (18) into (21) gives an approximate value for the new-time particle volume fraction:

$$\begin{aligned}
\tilde{\theta}_{\mathrm{p}\zeta}^{n+1} =& \tilde{\theta}_{\mathrm{p}\zeta} + \frac{\Delta t^2}{V_\zeta} \sum_{p} \frac{m_{\mathrm{p}} N_{\mathrm{p}} D_{\mathrm{p}}}{\rho_{\mathrm{p}}(1 + D_{\mathrm{p}} \Delta t)} \nabla S_\zeta(\tilde{\mathbf{x}}_{\mathrm{p}}) \cdot \mathbf{u}_{\mathrm{f,p}}^{n+1} \\
&+ \frac{\Delta t^2}{V_\zeta} \sum_{p} \frac{m_{\mathrm{p}} N_{\mathrm{p}}}{\rho_{\mathrm{p}}(1 + D_{\mathrm{p}} \Delta t)} \nabla S_\zeta(\tilde{\mathbf{x}}_{\mathrm{p}}) \cdot \boldsymbol{g} \\
&- \frac{\Delta t^2}{V_\zeta} \sum_{p} \frac{m_{\mathrm{p}} N_{\mathrm{p}}}{\rho_{\mathrm{p}}(1 + D_{\mathrm{p}} \Delta t)} D_{\mathrm{p}} \nabla S_\zeta(\tilde{\mathbf{x}}_{\mathrm{p}}) \cdot \mathbf{u}_{\mathrm{p}}^{n} \\
&- \frac{\Delta t^2}{V_\zeta} \sum_{p} \frac{m_{\mathrm{p}} N_{\mathrm{p}}}{\rho_{\mathrm{p}}^2(1 + D_{\mathrm{p}} \Delta t)} \nabla S_\zeta(\tilde{\mathbf{x}}_{\mathrm{p}}) \cdot \nabla p_{\mathrm{p}}^{n+1} \\
&- \frac{\Delta t^2}{V_\zeta} \sum_{p} \frac{m_{\mathrm{p}} N_{\mathrm{p}}}{\rho_{\mathrm{p}}^2 \theta_{\mathrm{p}}^{n}(1 + D_{\mathrm{p}} \Delta t)} \nabla S_\zeta(\tilde{\mathbf{x}}_{\mathrm{p}}) \cdot \nabla \tau_{\mathrm{p}}^{n+1}.
\end{aligned} \tag{22}$$

Abbreviated subscripts are used where ζ is the cell center node, ∇S_ζ is the gradient of the interpolation function, and $\mathbf{u}_{\mathrm{f,p}}^{n+1}$, $\nabla p_{\mathrm{p}}^{n+1}$ and $\nabla \tau_{\mathrm{p}}^{n+1}$ are fluid velocity, pressure and interparticle stress at particle locations, respectively. The implicit particle void fraction written in terms of coefficient is

$$\theta_{i,j}^{n+1} = \tilde{\theta}_{i,j} + \sum_{k=1}^{m} a_{i,j}^{k} p_{k}^{n+1} + \sum_{k=1}^{n} b_{i,j}^{k} u_{f,k}^{n+1} + \sum_{k=1}^{n} c_{i,j}^{k} v_{f,k}^{n+1} + \sum_{k=1}^{m-1} d_{i,j}^{k} \theta_{k}^{n+1} + C_{\theta_{i,j}}, \tag{23}$$

where a, b, c and d are coefficients defined from old time values, and the volume fraction is introduced through a linearized $\nabla\tau$. The new volume fraction depends on m neighbor pressures and volume fractions and n neighbor face center u_{f} and v_{f} velocities. The pressure and particle stress gradients defined from a bilinear interpolation give a 16 point stencil for pressure and volume fraction.

7. Calculation of polydisperse vertical suspensions

The bimodal suspension of a glass beads experiment given by Davis et al. (1982) is calculated by the MP-PIC method. The vessel is vertical as illustrated in Fig. 1. The fluid density and viscosity are 992 kg/m^3 and 0.0667 kg/(m-s), respectively. The small glass bead density is 2440 kg/m^3 and beads range in diameter from 125 to 150 μm. The larger bead density is 2990 kg/m^3 and beads range in diameter from 177 to 219 μm. The calculation uses a uniform random distribution of particle sizes between the reported experimental ranges. Initial volume fractions for the small and large beads are 3% and 1%, respectively. Specifications for the calculation are given in Table 1.

Table 1
Batch bimodal sedimentation (Davis et al. 1982)

Tilt	0°
Number of parcels particle 1	8000
Number of parcels particle 2	8000
Initial volume fraction particle 1	0.03
Initial volume fraction particle 2	0.01
Particle 1 radius (μm)	63
Particle 2 radius (μm)	89
Particle 1 density (kg/m^3)	2440
Particle 2 density (kg/m^3)	2990
Fluid density (kg/m^3)	992
P_s (pa)	50
β	2
θ_{cp}	0.6
x-gravity, y-gravity (m/s^2)	0,− 9.8
Number x-cells	5
Number y-cells	40
x-domain (cm)	5
y-domain (cm)	100
Fluid viscosity (kg/m-s)	0.0667
Max residual for θ_p, $\mathbf{u}_g$ and δp	10^{-10}

Fig. 4 shows the particle distribution at three times. Three regions can be observed. The top region is fluid, the next region is light particles and fluid, and the lower region contains fluid, light particles and heavy particles. Particles concentrate in the lower section of the vessel and approach the close-pack limit. Fig. 5 shows a one- and two-dimensional calculation of the transient interface levels compared with experimental data. The figure shows that the MP-PIC solution does well in calculating the vertical bimodal sedimentation.

8. Calculation of inclined sedimentation

The MP-PIC method is applied to the experiment given by Acrivo and Herbolzheimer (1979). The container was 5 cm wide and 40 cm high, and experiments were run with the container tilted at 0°, 20°, and 35°. The fluid density was 992 kg/m^3 and the viscosity was 0.0667 kg/(m-s). The particles were glass beads with a uniform random distribution of radii from 65 to 71 μm and density of 2420 kg/m^3. Calculations began with the container tilted (mixture-fluid interface was tilted at an angle to vessel walls). The height of the mixture height reported in this study, h, is illustrated in Fig. 6. Specifications for the MP-PIC calculation are given in Table 2.

The calculated particle distributions at 200 s for the container tilted 0°, 20° and 35° are shown in Fig. 7. Fig. 8 shows the particle volume fraction contours at times during the transient settling for the container tilted 35°. The MP-PIC calculation captures the physics of the Boycott settling problem. Below the downward-facing surface, a thin layer of near clear-fluid forms above the suspension which is illustrated by C in Fig. 2. The thin layer is seen in Fig. 7, and is more pronounced for the vessel tilted 35°. This wedge shaped layer is largest near

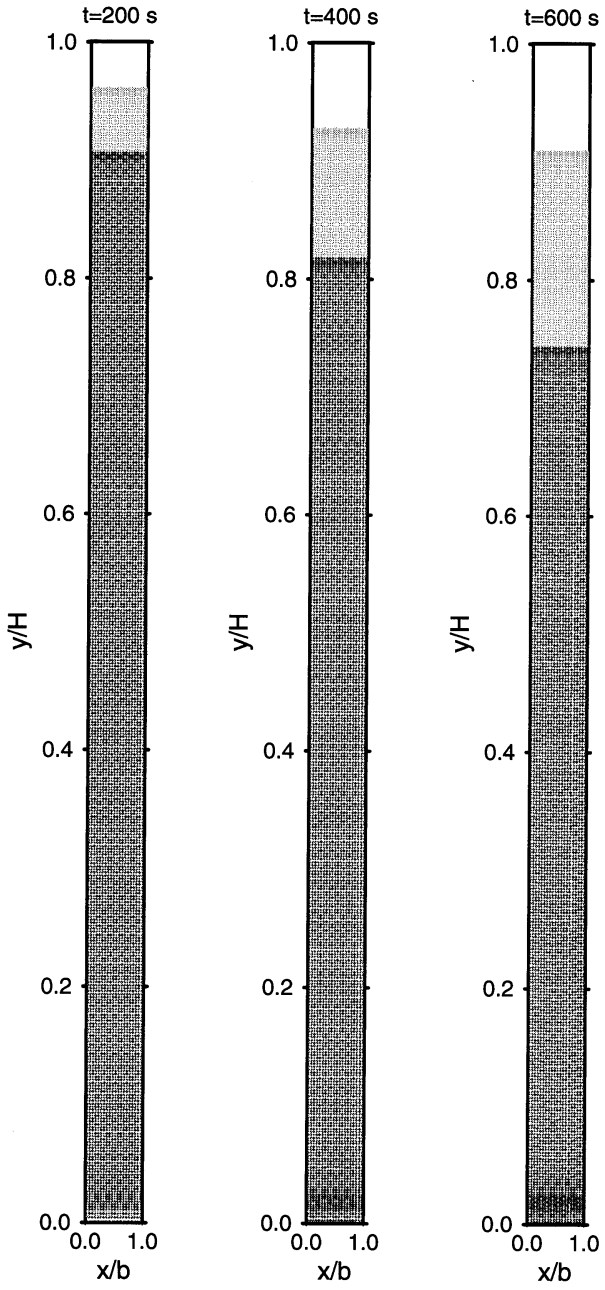

Fig. 4. Particle distribution for batch sedimentation (Davis et al., 1982). $H = 100$ cm and $b = 5$ cm.

the top, horizontal surface and decreases to zero in the lower part of the vessel where particles begin close-packing. The greater the incline of the vessel, the greater the clarified layer thickness. On the opposite, upward-facing surface, particles concentrate forming a wedge which corresponds to D in Fig. 2. Unlike the upper clarified region which is distinct, the lower dense

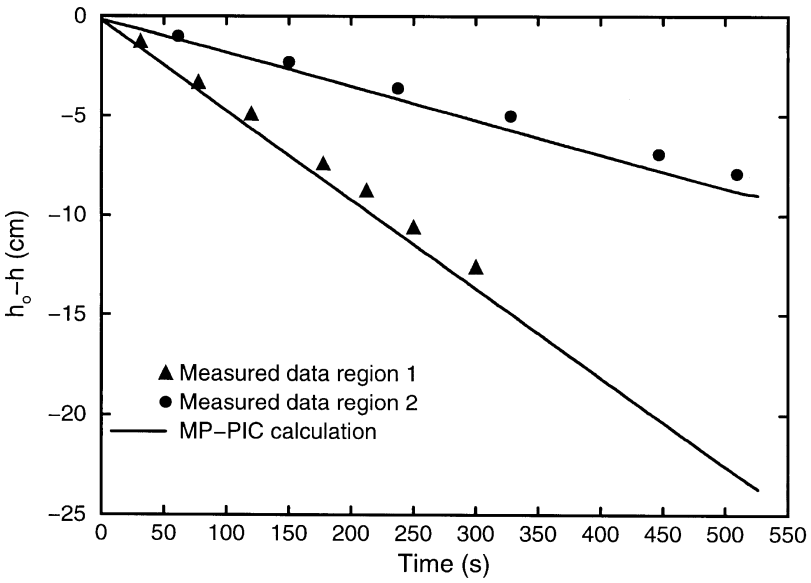

Fig. 5. Sedimentation levels from bimodal suspension of particles (Davis et al., 1982).

film gradient is not as steep. The dense particle layer is better seen in the particle volume fraction contours shown in Fig. 8. The calculated dense particle wedge is small near the top interface and becomes larger moving down in the container. The central region illustrated as B in Fig. 2 and seen in Figs. 7 and 8 is calculated to be homogeneous from the top horizontal interface stretching down in the container to where particles begin to close-pack. Fig. 9 gives the particle volume fraction across the channel (x-direction) and at three axial levels (y-direction). The time is 100 s. The curves overlay each other indicating the volume fraction is uniform axially and across the channel except near the walls. The clarified region at the top wall (right in the figure), is calculated to be nearly constant along the wall with a thickness of about 0.25 cm. Because the layer lies within two or three nodes, the calculation is not expected

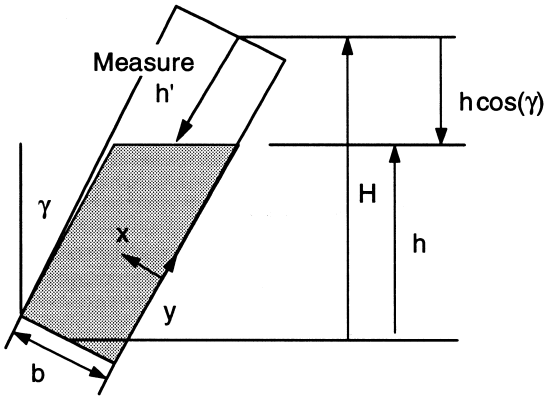

Fig. 6. The height of sedimentation reported from calculations.

Table 2
Batch sedimentation. Container tilted 0°, 20° and 35°

Tilt	0°	20°	35°
Number of parcels	8000	18111	18111
Initial particle volume fraction	0.1	0.1	0.1
Particle radius (μm)	65–71	65–71	65–71
Particle density (kg/m^3)	2420	2420	2420
Fluid density (kg/m^3)	992	992	992
P_s (pa)	75	100	100
β	2	3	3
θ_{cp}	0.7	0.6	0.6
x-gravity, y-gravity (m/s^2)	0, −9.8	−3.35, −9.21	−5.62, −8.027
Number x-cells	5	20†	20†
Number y-cells	40	50	50
x-domain (cm)	5	5	5
y-domain (cm)	40	42	42
Fluid viscosity (kg/m-s)	0.0667	0.0667	0.0667
Max residual for θ_p, $\mathbf{u}_g$ and δp	10^{-8}	10^{-7}	10^{-7}

†Nonuniform x-interval varying from $\Delta x = 0.158$ cm at wall to $\Delta x = 0.297$ cm at the center

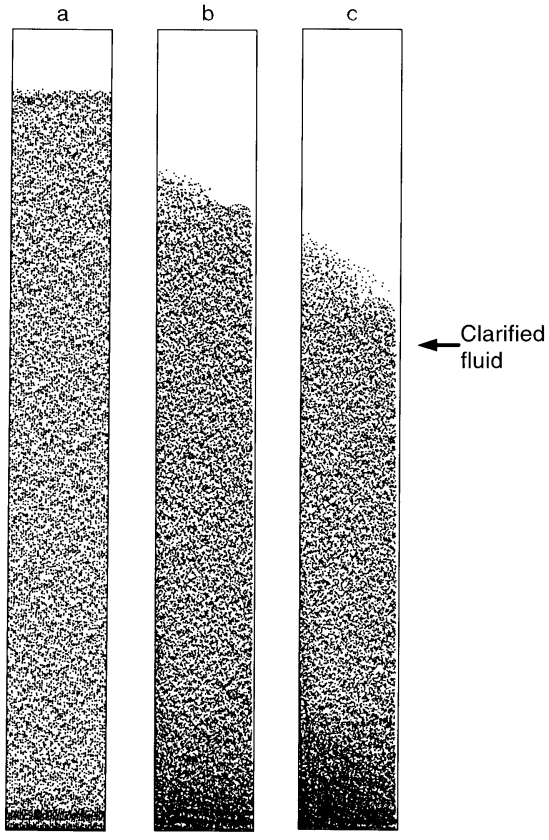

Fig. 7. The particle distributions for batch sedimentation at 200 s. (a) Tilted 0°; (b) tilted 20°; and (c) tilted 30°.

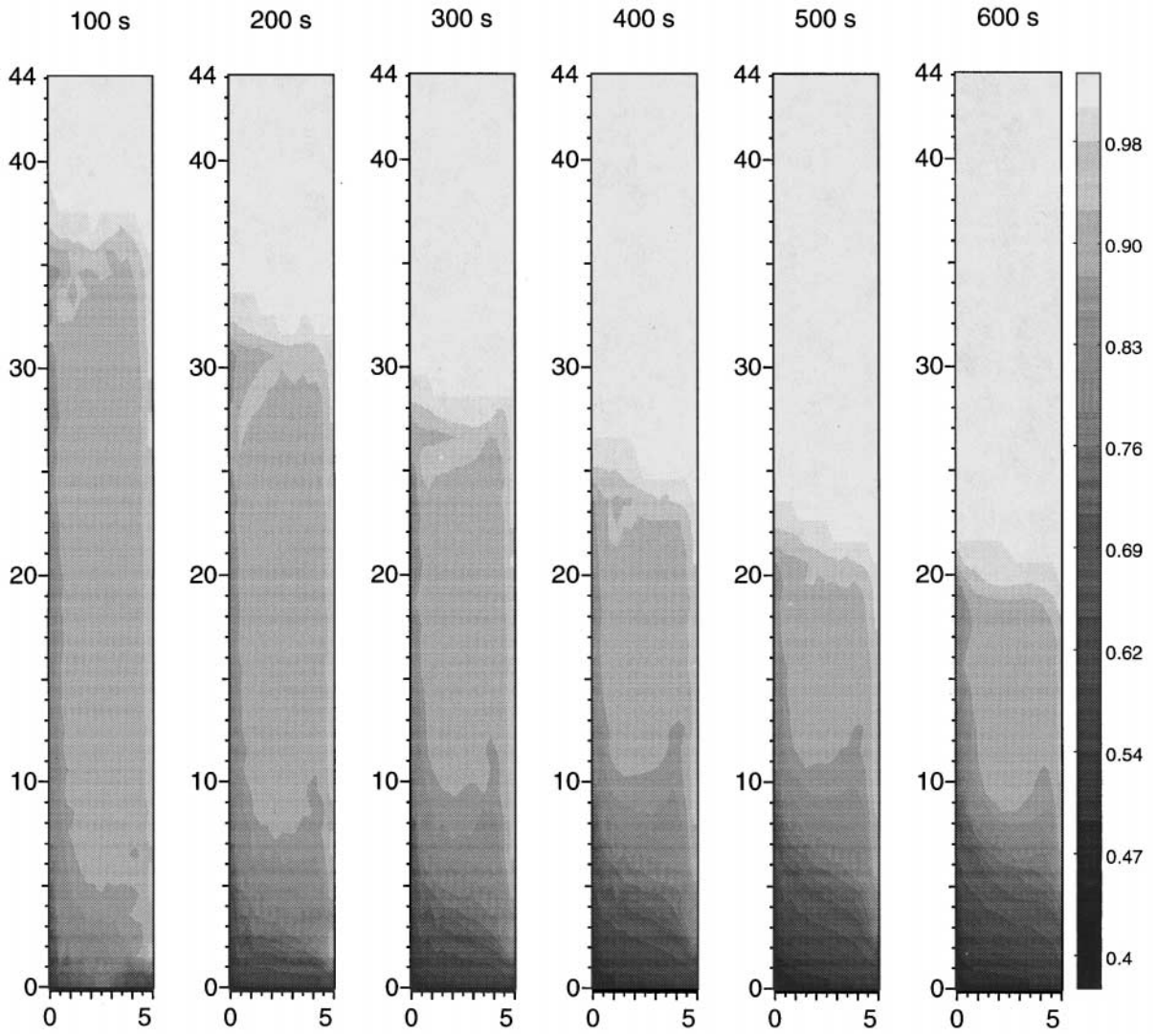

Fig. 8. Volume fraction of particles in batch sedimentation for a container tiled at 35°.

to capture details of the clarified region. However, the thickness which is calculated compares reasonably with the measured thickness of 0.1–0.25 cm given by Acrivos and Herbolzheimer (1979). The layer of dense particles on the upward facing wall (left in the figure) is calculated to range from 0.5 to 0.65 cm wide.

The small particles with average radius of 68 μm in the viscous fluid produces Reynolds numbers less than 0.03 and a high particle drag coefficient of $C_D > 30\ 000\ s^{-1}$ which tightly couples particles and fluid. Unlike the sedimentation in a vertical vessel, where particles slowly descend through the fluid, particles in the inclined sedimentation are swept upward by rising fluid along the top wall. Likewise the fluid is dragged along with particles flowing down the bottom wall. The fluid velocity field for the 35° tilted container at time intervals is shown in

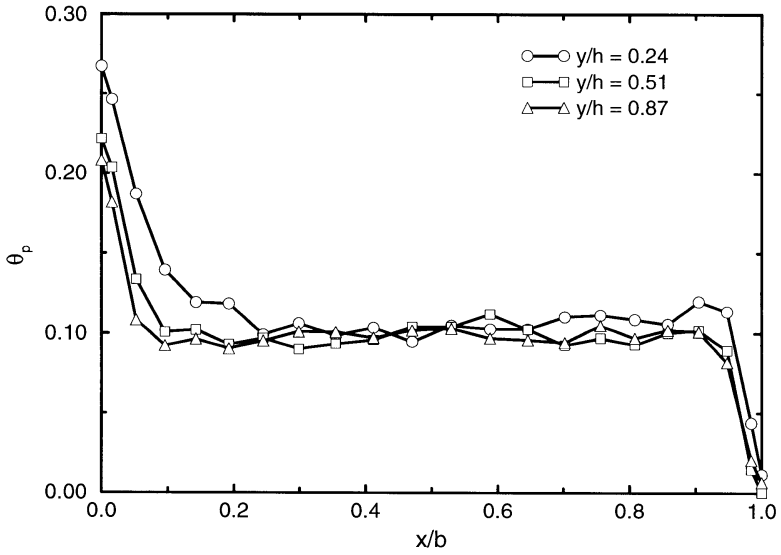

Fig. 9. Particle volume fraction distribution across the channel for the container tilted 35° at 100 s.

Fig. 10. Velocities less than 0.1 cm/s are not shown in the figure. A vortex pattern is calculated to form. The large drag coefficient gives a particle velocity near the same magnitude as the fluid velocity.

Velocities are largest near the walls with fluid flowing upward under the downward-facing surface, and a dense mixture flowing down the upward-facing surface. A vortex pattern was observed in experiments by Kinosita (1949). Kinosita measured particle velocities as high as 100 times Stokes velocity. Hill et al. (1977) calculated and measured particle velocities on the order of 10 times Stokes velocity. The MP-PIC calculated velocities are large at the start of sedimentation and decrease as particles settle out of solution. The MP-PIC calculation produced maximum particle velocities on the order of 20 times Stokes velocity for the 35° tilted container. Decreasing the fluid viscosity from 0.0667 to 0.0188 (kg/(m-s) increased the fluid velocity in the clarified layer by about two. The lower fluid viscosity matches the fluid used by Herbolzheimer (1983).

Fig. 11 compares the measured and MP-PIC calculated transient settling rates for the container tilted 0°, 20° and 35°. The MP-PIC calculations compares well with the measured vertical and inclined sedimentation rate data.

9. Instability at the upper clarified liquid interface

The interface between rising clarified fluid and particle mixture can form instabilities similar to those of a fluid flowing down an inclined plate. Herbolzheimer (1983) presented photographs of Kelvin–Helmholtz type waves at the interface. He observed that almost immediately after an experiment started waves formed in the upper portion of the channel and traveled up along the interface between the pure fluid and the mixture. The waves, once they

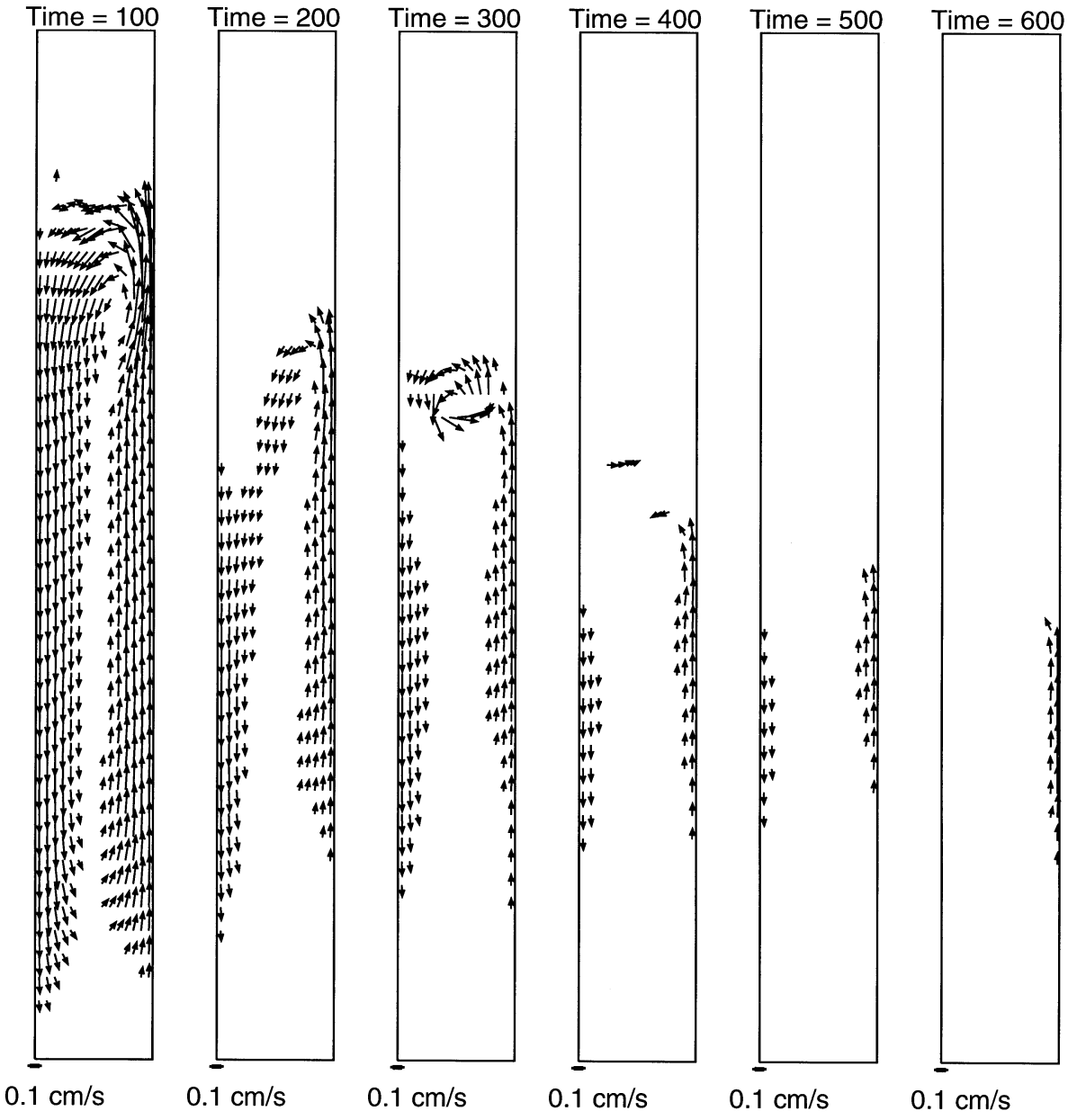

Fig. 10. Fluid velocity for container tilted 35°.

appeared, grew rapidly with amplitude comparable to the thickness of the clear fluid layer. The instabilities occurred for the vessel at small angles of inclination and were not present at large angles. Herbolzheimer found the experimentally observed instabilities follow the general trends predicted by linear stability analysis, but he was unable to quantitatively compare his analysis with experimental data. The MP-PIC calculation for the vessel tilted 35° predicted low amplitude waves early in the settling transient which lasted only a short time. Acrivos and

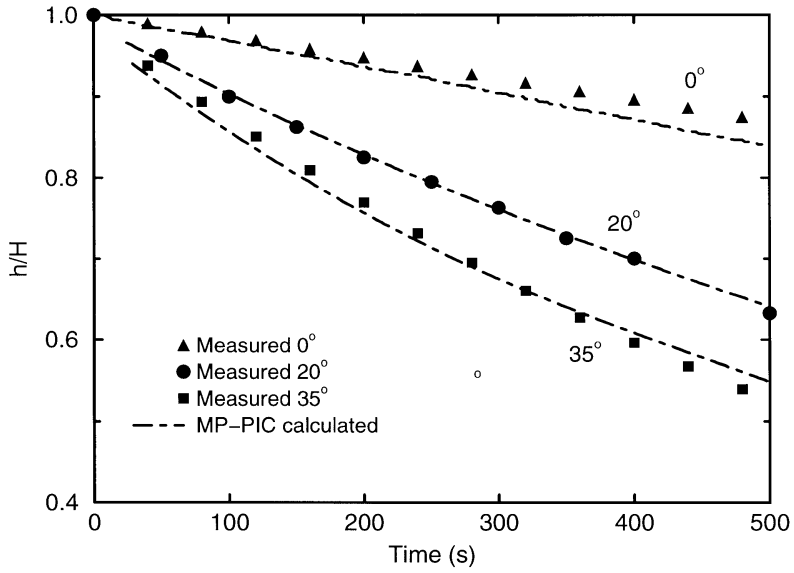

Fig. 11. MP-PIC calculated and measured interface for suspension of particles. Measured data from Acrivos and Herbolzheimer (1979).

Herbolzheimer (1979) did not report instabilities for their experiment. A calculation was done using the fluid properties from Herbolzheimer's (1983) experiment with the primary difference from Acrivos and Herbolzheimer (1979) experiment being a lower fluid viscosity. The calculation was made with fluid viscosity 0.0188 kg/(m-s) (used in the interphase drag), particle radius 66 μm, and particle density 2440 kg/m^3. For the vessel tilted 20°, calculated instabilities occurred early in the transient, and the wave amplitude was on the order of the clarified layer thickness which was much larger than that seen in the calculation with the higher viscosity. Fig. 12 shows the calculated particle distribution compared with the photographed mixture. The calculated waves travel up the under side of the top wall, and within a minute, the waves subside and the clarified fluid–particle interface becomes stable. Herbolzheimer observed instabilities in the continuous sedimentation, and no time period for the presence of waves, as occurs in batch sedimentation, was given. A second calculation was made with the vessel tilted at a large inclination of 55°. As in the experiment, no waves formed. Fig. 12 shows the calculated particle distribution for the vessel tilted 55° compared with a photograph of the sedimentation.

The calculated particle volume fraction (θ_p) and axial fluid velocity near the upper wall are shown in Fig. 13 and reflect the observed instabilities. The clear fluid, with $\theta_p = 0$, flows next to the top wall, with waves periodically reaching the wall. The wavy region is considerably larger than the calculated stable clarified region thickness. The fluid velocity, in the clarified region is disrupted by the waves of particles. The clarified fluid velocity cyclically drops from above 3.5 to less than 2 cm/s as waves of particles move into the clarified fluid layer. Measuring the distance between peaks in Fig. 14, the wavelength at 14 s is about 5 cm.

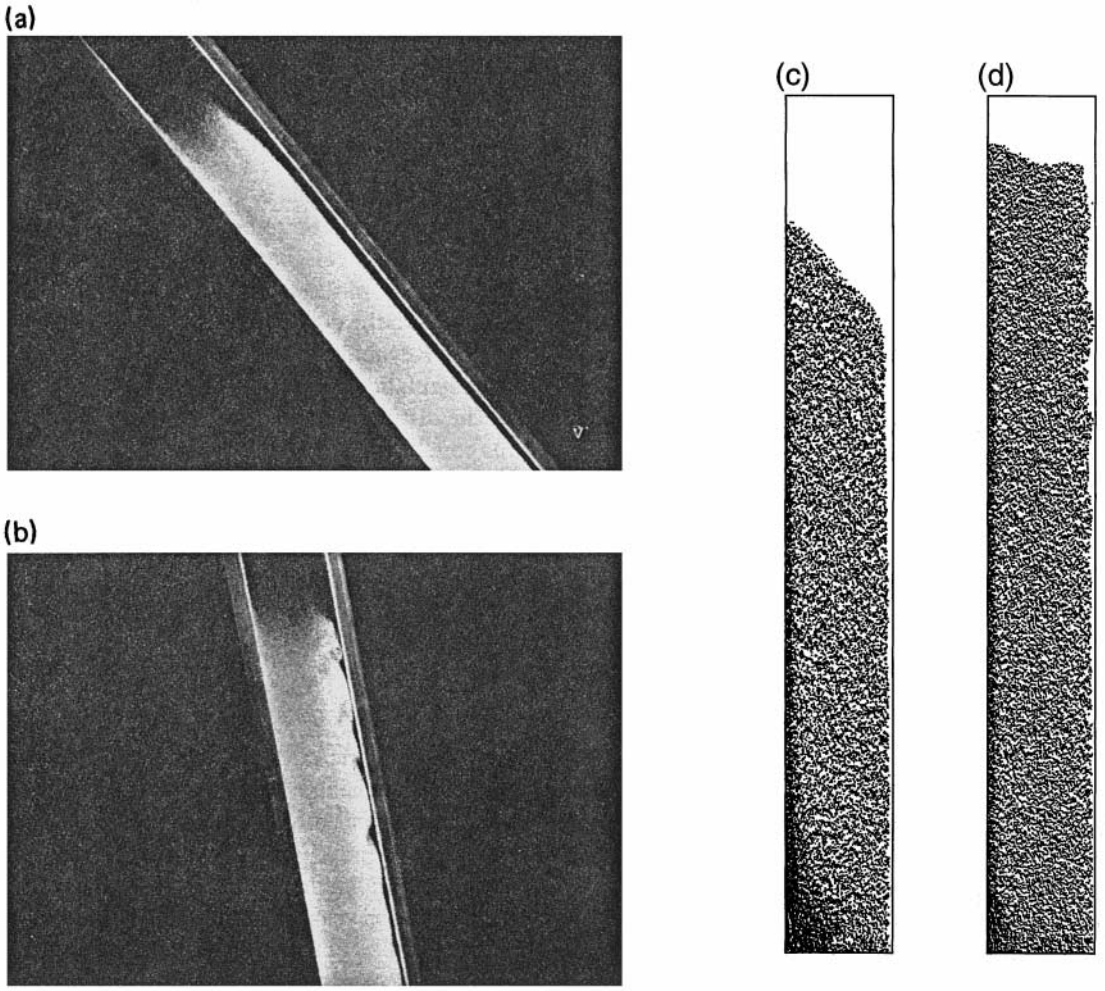

Fig. 12. Observation of the flow for a volume fraction of 0.01 and fluid viscosity of 18.8 cP. (a) Large angle of inclination; (b) angle is decreased and waves appear along interface in the upper region of channel. Reprinted with permission from Herbolzheimer, E., 1983, "Stability of the flow during sedimentation in inclined channels," *Phys. Fluids*, vol. 26, Fig. 2, p. 2044. Copyright 1983 American Institute of Physics; (c) calculated sedimentation at 20.5 s with vessel tilted 55°; (d) calculated sedimentation at 14.75 s with vessel tilted 20°.

10. Particle stress

The calculations are not tuned to calculate the sedimentation problem. The interphase drag is a standard constitutive equation used in droplet flow. The particle stress is a simple model which neglects off diagonal terms in the stress tensor. The diagonal element of the stress tensor is modeled by isotropic stress given by (9),

$$\tau = \frac{P_s \theta_p^{\beta}}{\theta_{cp} - \theta_p}.$$

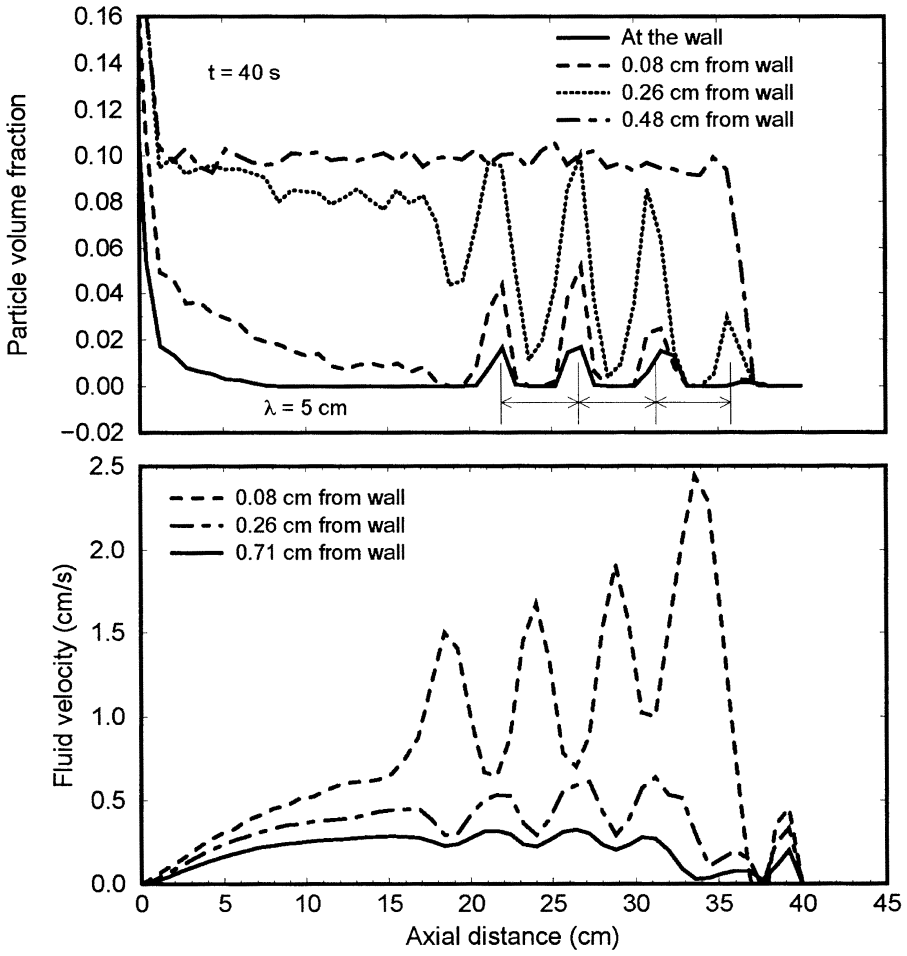

Fig. 13. Particle volume fraction and fluid velocity at 14 s. Vessel inclined 20°, viscosity 0.0188 kg/(m-s), particle radius 66 μm, and particle density 2440 kg/m^3.

The two constants, P_s and β, in this empirical model are not well defined. The choice for the value of β and P_s used in this work is discussed below.

The purpose of the particle stress is to provide a pressure type force which prevents packing of particles beyond a limit (close-pack volume fraction, θ_{cp}). The model captures the essence of repelling particles from cells where the particle volume fraction is large, but the model does not consider the influence of particle velocities and particle sizes. The inclusion of off diagonal terms and more complete modeling is relegated to future work. The P_s term is not necessary to provide a static balance between $\nabla\tau$ and the hydrostatic head (considering particles as a fluid). However, the model has a singularity at close-pack, and the stress gradient is very steep near the singularity. The P_s term stretches the gradient giving a more stable approach to close-pack. In the dynamic case, the particle stress retards the momentum of dynamic particles encroaching on a dense particle region. If the particle stress is insufficient to slow and repel a dynamic particle entering a region near close-pack, over a finite time step, the small change in

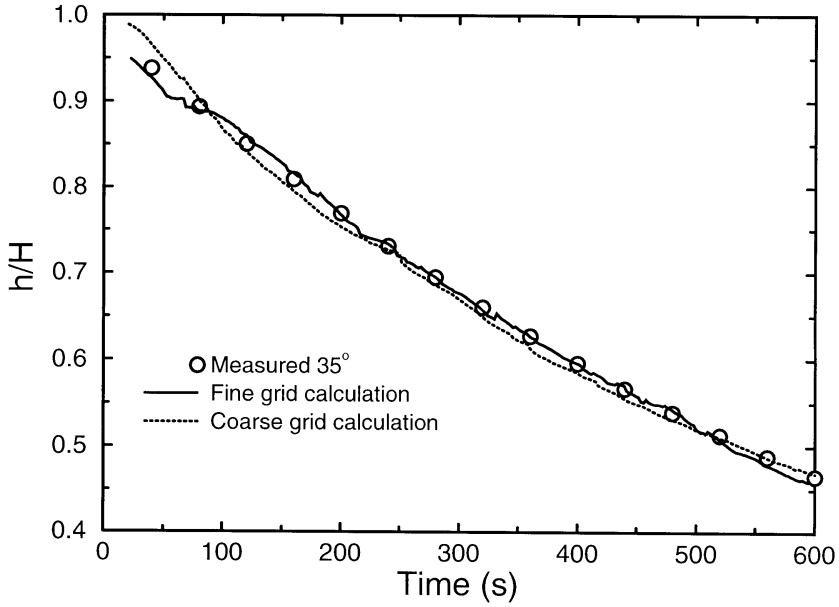

Fig. 14. Batch sedimentation rate for container tilted 35° for fine and coarse grids.

volume fraction near the singularity can produce a large stress gradient, which blows apart the particle bed. Further, in the numerical model, the particle solids stress acts as a stabilizing force on oscillations similar to the surface tension in the classic Kelvin–Helmholtz problem or the density in buoyancy stratified flow. The interface pressure from surface tension tends to restore the interface to a stable state. Similarly in the numerical sedimentation problem, a large particle stress damps instabilities at the interface between the particle-mixture and fluid, and prevents waves from forming.

The normal particle stress model needs to limit the volume fraction to less than the close-pack value, but not have an overly diffusive nature at low to moderate volume fractions. To retain the advantage of stretching the particle stress gradient near the singularity (use of a large P_s) which reduces numerical difficulties, and not have excessive stress gradients at low volume fraction, the power, β, is applied to the particle volume fraction in Eq. (9). It can be shown that using $\beta = 3$, P_s can range from 1 to 100 Pa and the calculated results are the same in the low volume fraction region which includes the clarified layer width where instabilities may form. On the other hand, if $\beta = 1$ and $P_s > 8$ Pa the instabilities are damped. Therefore, by using $\beta = 3$ in this study, the calculated low volume fraction region ($\theta_p < 20\%$) is insensitive to P_s and $\nabla\tau$, while near close-pack, a value of $P_s = 100$ Pa provides a stable solution.

11. Grid independence

In particle solutions, the grid cell size should be large enough to contain a number of particle parcels. The grid must also be fine enough to resolve the physics of the problem. A check is made to evaluate the influence of the grid on the sedimentation calculations. Results

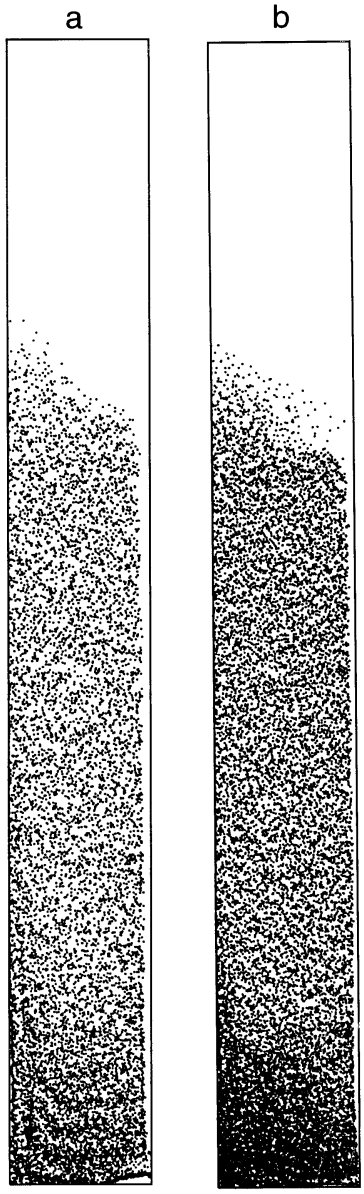

Fig. 15. Particle distribution for container tiled 35° for fine and coarse grids. (a) Coarse grid; (b) fine grid.

from a coarser grid with fewer parcels is compared to results from the finer grid used in this study. The calculation was for a vessel tilted 35°, and the properties of the calculations are given in Table 2 except for differences listed in Table 3. Fig. 14 shows the sedimentation rate for the two calculations is the same, and Fig. 15 shows that the particle distribution has the same appearance. This suggests that the grid resolution or number of parcels does not unduly influence the calculations in this study.

Table 3
Difference between coarse and fine grid. Container tilted 35°

	Coarse	Fine
Nodalization (x by y)	16×30	20×50
Number of parcels	12000	20000

12. Concluding remarks

The MP-PIC numerical method performs well predicting sedimentation problems. The Lagrangian–Eulerian numerical approach allows calculation of dilute particle flow to dense close-pack particles. The application to vertical bimodal sedimentation illustrated the ability to calculate the sedimentation of two sizes of particles. Further, an advantage of the MP-PIC scheme, is that there is practically no limit to the number of sizes and densities of particles which can be modeled.

There was no tuning of the MP-PIC calculation for batch sedimentation. The interphase drag (related to a particle hindrance function) was a general expression used in droplet flow. A standard particle stress model was used where the particle stress was shown to be insensitive to the P_s constant in the model at low to moderate volume fraction providing that $\beta = 2$ or 3. Approaching close-pack, the P_s stretches the steep gradient near the singularity giving a smoother numerical solution.

The calculated settling rate for both the vertical, bimodal solution and the inclined mixtures compare well with measured data. The MP-PIC solution predicted the physics of both the slow vertical sedimentation and the more dynamic inclined sedimentation. In inclined sedimentation, a clarified layer was predicted at the upper wall, and a dense particle layer was predicted at the lower wall. Circulation currents were calculated in the vessel and the particle distribution was homogenous except near walls and at the vessel bottom where particles settled out of solution.

The MP-PIC method also predicted instabilities at the interface between clarified fluid and mixture. A weak instability was calculated for the experiments by Acrivos and Herbolzheimer (1979). By lowering the viscosity to the value used in experiments by Herbolzheimer (1983), instabilities were calculated which were similar to those measured. Instabilities formed at the start of sedimentation, but died out as velocities decreased with time.

References

Acrivos, A., Herbolzheimer, E., 1979. Enhanced sedimentation in settling tanks with inclined walls. Journal of Fluid Mechanics 92, 435–457.

Al-Naafa', M.A., Selim, M.S., 1989. Sedimentation of polydisperse concentrated suspensions. The Canadian Journal of Chemical Engineering 67, 253–263.

Amsden, A.A., O'Rourke, P.J., Butler, T.D., 1989. KIVA-II: A computer program for chemically reactive flows with sprays. LA-11560-MS, Los Alamos National Laboratory.

Anderson, D.A., Tannehill, J.C., Pletcher, R.H., 1984. Computational Fluid Mechanics and Heat Transfer. Hemisphere, New York.

Andrews, M.J., O'Rourke, P.J., 1996. The multiphase particle-in-cell (MP-PIC) method for dense particle flow. International Journal of Multiphase Flow 22, 379–402.

Auzerais, F.M., Jackson, R., Russel, W.B., 1988. The resolution of shocks and the effects of compressible sediments in transient settling. Journal of Fluid Mechanics 195, 437–462.

Batchelor, G.K., 1988. A new theory of the instability of a uniform fluidized bed. Journal of Fluid Mechanics 193, 75–110.
Boycott, A.E., 1920. Sedimentation of blood corpuscles. Nature 104, 532.
Davis, R.H., Acrivos, A., 1985. Sedimentation of noncolloidal particles at low Reynolds numbers. Annual Review of Fluid Mechanics 17, 91–118.
Davis, R.H., Herbolzheimer, E., Acrivos, A., 1982. The sedimentation of polydisperse suspensions in vessels having inclined walls. International Journal of Multiphase Flow 8 (6), 571–585.
Gidaspow, D., 1986. Hydrodynamics of fluidization and heat transfer: supercomputer modeling. Applied Mechanics Review 39, 1–22.
Gidaspow, D., 1994. Multiphase Flow and Fluidization Continuum and Kinetic Theory Description. Academic Press, Boston, MA.
Harris, S.E., Crighton, D.G., 1994. Solutions, solitary waves and voidage disturbances in gas-fluidized beds. Journal Fluid Mechanics 266, 243–276.
Herbolzheimer, E., 1983. Stability of the flow during sedimentation in inclined channels. Physics of Fluids 26, 2043–2045.
Hill, W.D., Tothfus, R.R., Li, K., 1977. Boundary-enhanced sedimentation due to settling convection. International Journal of Multiphase Flow 3, 561–583.
Kapoor, B., Acrivos, A., 1995. Sedimentation and sediment flow in settling tanks with inclined walls. Journal of Fluid Mechanics 290, 39–66.
Kinosita, K., 1949. Sedimentation in tilted vessels. Journal of Colloid Interface Science 4, 166–176.
Mirza, S., Richardson, J.F., 1978. Sedimentation of suspensions of particles of two or more sizes. Chemical Engineering Science 34, 447–454.
Nakumura, H., Kuroda, K., 1937. La cause de l'acceleration de la vitesse de sedimentation des suspension dans les recipents inclines. Keijo. J. Med. 8, 256–296.
O'Rourke, P.J., 1981. Collective drop effects on vaporizing liquid sprays. Ph.D thesis, Princeton University.
Patankar, S.V., 1980. Numerical Heat Transfer and Fluid Flow. Hemisphere, New York.
Ponder, E., 1925. On sedimentation and rouleaux formation. Quarterly Journal of Experimental Physiology 15, 235–252.
Richardson, J.F., Zaki, W.N., 1954. Sedimentation and fluidization: Part I. Transactions of the Institution of Chemical Engineers 23, 35–53.
Risk, M.A., 1993. Mathematical modeling of densely loaded particle laden turbulent flows. Atomization and Sprays 3, 1–27.
Shih, Y.T., Gidaspow, D., Wasan, D.T., 1987. Hydrodynamics of sedimentation of multisized particles. Powder Technology 50, 201–215.
Snider, D.M., O'Rourke, P.J., Andrews, M.J., 1997. An incompressible two-dimensional multiphase particle-in-cell model for dense particle flows, LA-13280-MS. Los Alamos National Lab., Los Alamos, NM.
Williams, F.A., 1985. Combustion Theory. 2nd. Benjamin/Cummings, Menlo Park, CA.